Reprint from SPIE's Proceedings, Volume 4980, Reliability, Testing, and Characterization of MEMS/MOEMS, San Jose, CA, January, 2003 pp 22-40.

Wear Mechanisms in a Reliability Methodology (*Invited*)

Danelle M. Tanner* and Michael T. Dugger
Sandia National Laboratories

ABSTRACT

The main thrust in any reliability work is identifying failure modes and mechanisms. This is especially true for the new technology of MicroElectroMechanical Systems (MEMS). The methods are sometimes just as important as the results achieved. This paper will review some of the methods developed specifically for MEMS. Our methodology uses statistical characterization and testing of complex MEMS devices to help us identify dominant failure modes. We strive to determine the root cause of each failure mode and to gain a fundamental understanding of that mechanism. Test structures designed to be sensitive to a particular failure mechanism are typically used to gain understanding. The development of predictive models follows from this basic understanding.

This paper will focus on the failure mechanism of wear and how our methodology was exercised to provide a predictive model. The MEMS device stressed in these studies was a Sandia-developed microengine with orthogonal electrostatic linear actuators connected to a gear on a hub. The dominant failure mechanism was wear in the sliding/contacting regions. A sliding beam-on-post test structure was also used to measure friction coefficients and wear morphology for different surface coatings and environments. Results show that a predictive model of failure-time as a function of drive frequency based on wear fits the functional form of the reliability data quite well, and demonstrates the benefit of a fundamental understanding of wear. The results also show that while debris of similar chemistry and morphology was created in the two types of devices, the dependence of debris generation on the operating environment was entirely different. The differences are discussed in terms of wear maps for ceramics, and the mechanical and thermal contact conditions in each device.

Keywords: MEMS Reliability, Reliability Methodology, Failures, Wear in humid environments, Wear, Wear Maps

1. INTRODUCTION

A high-volume MEMS manufacturer such as Analog Devices uses a model of efficient production and test for a reliable cost-effective product.[1] They successfully integrate process engineering, design, yield engineering, reliability, characterization, and test from the early development phases through product release. High-volume production provides the raw statistical data to study small-scale problems. However, not all researchers have access to such a large database. In another paper, Arney[2] describes the fourfold mission of MEMS reliability research as a) obtaining a fundamental understanding of the die-level failure mechanisms, b) facilitating the design, packaging, and testing of commercially interesting MEMS devices, c) previewing the qualification and compliance testing of the device, and d) ensuring long-term reliability of MEMS products in the field.

The objective of this paper is to show how all the components of a reliability methodology (shown in Figure 1) fit together to yield a reliability model. The focus here is on only one failure mechanism, wear of contacting surfaces. The discussion is constrained to die-level reliability, knowing full well that for a final product, all aspects of fabrication, packaging, system integration, and manufacturing must be considered. It is important to acknowledge that there can be failure modes associated with friction, for example, a high static friction coefficient that prevents operation of the device, or an increase in dynamic friction with age such that drive signals designed at the time of fabrication are at some later time insufficient to operate the device. It should also be noted that friction and wear are coupled phenomena, since

---

* Contact Info: tannerdm@sandia.gov; phone 505-844-8973; fax 505-844-2991; http://www.mems.sandia.gov; Sandia National Laboratories, PO Box 5800 MS-1081, Albuquerque, NM, USA 87185-1081

friction provides the shear force at the surface necessary to cause material damage and removal, and this material damage will influence the subsequent friction forces. Device and test structure data are shown that reveal the basic understanding needed to develop a predictive reliability model.

Wear is a very complex phenomenon, involving not only the mechanical properties and chemistry of the bodies in contact, but also the pressure and interfacial velocity under which these bodies make contact, and the other species (such as lubricant layers or gases) present in the environment in which they function. These factors govern not only the rate of wear, but also the mechanism by which material is removed, the worn surface morphology and debris characteristics.

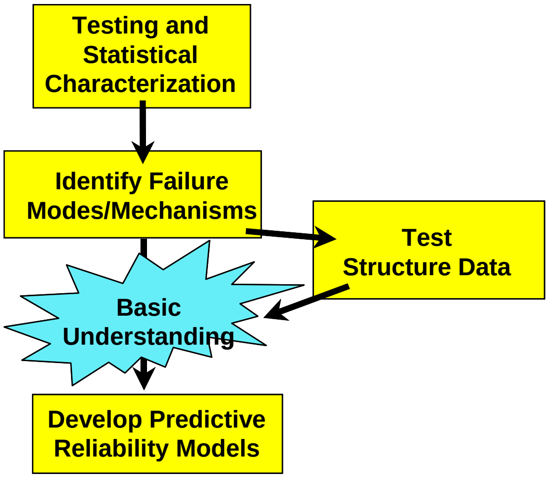

Figure 1: The basic components of a reliability methodology.

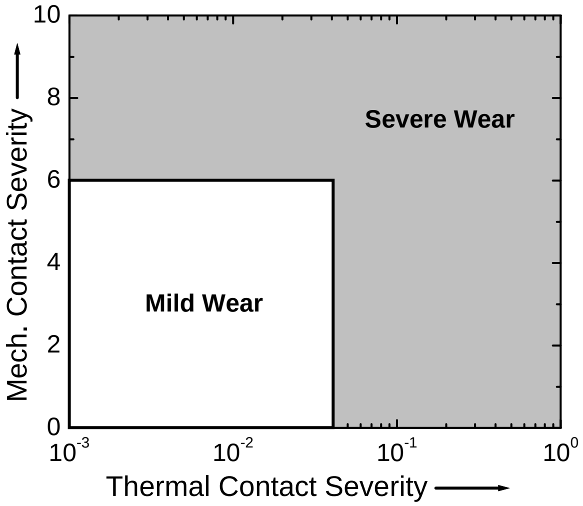

Figure 2. Schematic wear mechanism map for ceramics, in terms of mechanical and thermal severity of contact, after Adachi et al.

Lim and Ashby[3] developed a method for graphically depicting the relationships between competing wear mechanisms and how they changed with operating parameters in a wear map. This approach was first applied to steels, where they experimentally and theoretically identified regimes of different wear mechanism in a parameter space of normalized pressure versus normalized velocity. In this case, pressure is normalized by taking the ratio of contact pressure to the mechanical strength of the materials in contact, and normalized velocity is the ratio of the rate of heat generation at the contact to heat transfer away from the contact. More recently, Adachi et al.[4] used a similar approach to map wear mechanisms in ceramics, in a parameter space defined by the mechanical and thermal severity of contact. A wear map for ceramics is shown schematically in Figure 2. Mild wear produces a relatively smooth worn surface with a specific wear amount, w_s, less than 10^{-6} mm^3 (Nm)$^{-1}$ and severe wear produces a relatively rough worn surface with w_s larger than 10^{-6} mm^3 (Nm)$^{-1}$.

Thermal contact severity is defined as

$$S_{c,t} = \left(\frac{\gamma\mu}{\Delta T_s} \sqrt{\frac{vWH}{k\rho c}} \right) \tag{1}$$

where γ is the heat partition ratio (amount of thermal energy transferred to body 1 versus body 2), μ is the friction coefficient, ΔT_s is the thermal shock resistance (in Kelvin), W is the contact load, H is the hardness, k is the thermal conductivity, ρ is the density and c is the specific heat of the material. Similarly, mechanical contact severity is defined as

$$S_{c,m} = \frac{(1+10\mu)P_{\max}\sqrt{d}}{K_{IC}} \tag{2}$$

where $P_{\max}$ is the maximum Hertzian contact pressure, d is the length of any pre-existing crack and K_{IC} is the fracture toughness of the material, Both of these contact severity parameters are dimensionless.[4]

Examining changes in wear mechanism using wear mechanism maps typically involve variation in contact force, sliding speed, roughness, or material properties, with the environment held constant. It should be noted that the environment may dramatically influence the wear mechanism and debris morphology. Therefore, wear mechanism regimes may be considered to exist in three dimensions, where the third dimension represents changes in the chemistry of surfaces due to reaction with the environment. Fischer and Mullins[5] have described the types of interactions with the environment that may affect wear of ceramics, and conclude that chemical reactions that are influenced by the presence of friction, so-called "tribochemical" reactions, can either increase or decrease wear rate depending upon the environment and contact conditions.

2. DEVICE AND TEST STRUCTURE DATA

For many MEMS devices, especially actuators, normal operation requires surfaces to come into contact and rub against one another. The initial friction coefficients, and changes in friction with age or operation, are factors that affect initial and long-term reliability. Wear of the rubbing surfaces is also an important factor determining long-term reliability of devices. One of the first experiments to show wear as a dominant failure mechanism, by Gabriel et al. [6] ran polysilicon microturbines[7] and gears at rotational speeds up to 600,000 rpm. A focused air jet directed at the turbine induced the rotation. They estimated dynamic coefficients of friction between polysilicon and silicon ranging in value from 0.25 to 0.35. Wear was extensive enough to cause misalignment followed by wedging of the device.

In another experiment, microfabricated radial-gap electric motors were tested in room air at speeds between 200 and 2000 rpm.[8] Lifetime was limited by wear to 10,000 cycles. This experiment incorporated a silicon nitride film in the bearing and measured a coefficient of friction of the nitride-polysilicon bearing to be 0.36. Scanning electron microscopy (SEM) analysis after failure revealed wear particles on the friction bearing surfaces.

In the discussion that follows, we will review experiments on a device and a test structure. The device is a complex system of electrostatic actuators that rotate a gear on a hub. The test structure is a friction tester designed to measure the coefficient of friction between two polysilicon surfaces. Our goal is to examine the data from both and try to understand from a fundamental level their similarities and differences.

2.1 Description and Testing Methods

2.1.1 Microengine

The device used in this comparison was the electrostatically driven microactuator (microengine) developed at Sandia National Laboratories [8]. The microengine consists of orthogonal linear comb drive actuators mechanically connected to a rotating gear as seen in Figure 3. By applying voltages, the linear displacement of the comb drives is transformed into circular motion. The linkage arms are connected to the gear via a pin joint. The gear rotates about a hub, which is anchored to the substrate.

Model-based drive signals for microengines were derived previously[9] and a software code[10] was developed to provide the properly timed voltage signals to the actuators. The code provides an interface to set various parameters in the drive signals. Two of these parameters are radial force and longitudinal force that the actuators provide to the pin joint. We typically set the radial force to zero and the microengine will operate with a longitudinal force as low as 1 μN.

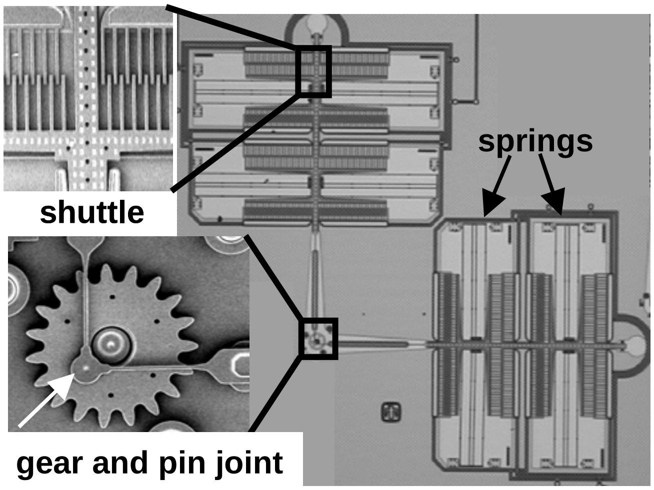

Figure 3. SEM image of the microengine. The shuttle and comb fingers are shown in the upper inset. The lower inset shows an enlarged view of the output gear (diameter of 80 μm) and the location of the pin joint.

Our largest acceleration parameter is drive frequency. Under an operating condition of 500 Hz or less the majority of microengines with symmetric actuators will rotate for roughly 10^9 cycles before failure due to wear/adhesion in the pin joint.[11] However, at higher frequencies (up to 3000 Hz) the number of cycles to failure is reduced by 3 to 4 orders of magnitude. This effect[12] is probably due to additional force exerted on the pin joint at the higher frequencies. Observation using strobe and imaging techniques[13] of the linkage arms from a gearless microengine showed circular motion for frequencies below 500 Hz. However, at higher frequencies the circular motion was elongated into an oval indicating that some additional force was present. This additional force is most likely due to an absence of the proper dynamic terms in the model.

2.1.2 Sidewall Friction Tester

The friction forces at micromachine contacts are difficult to explore with complex devices such as the Sandia microengine. Consequently, the sidewall friction structure was designed to permit quantitative measurement of friction forces and to simplify the contact geometry so that observations could be associated with a known contact pressure in an isolated region of the surface. This device can be used to examine the performance of surface treatments, effects of environment, contact pressure, interfacial velocity, etc.

The sidewall friction device is shown in Figure 4. The device consists of two orthogonal electrostatic comb actuators connected to a movable beam. A post is formed by etching through sacrificial oxide layers so that a polysilicon deposition forms a structure that is anchored to the substrate and has a cylindrical geometry facing the beam. A SEM picture of the beam and post in their rest positions is shown in Figure 4(b). Applying a DC voltage brings the beam into contact with the post, and then applying a waveform to the other actuator causes the beam to slide against the post. When actuated with a square wave, we measure the amplitude of the beam motion for a given voltage (force) applied to the loading comb. To obtain displacement amplitude, images are captured when the beam is at opposite ends of travel. This process is repeated for several successive cycles. The images are processed to extract the time displacement amplitude of the beam.

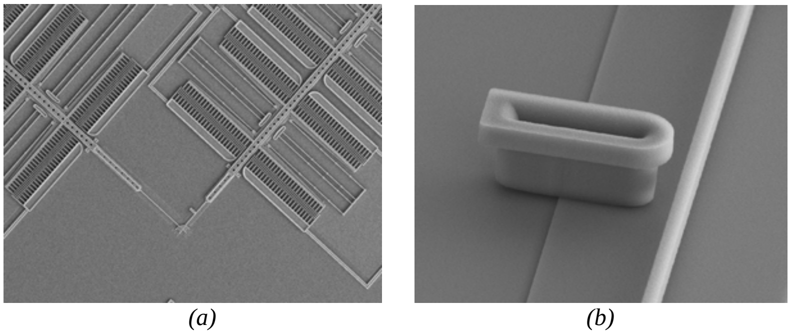
(a) (b)

Figure 4. Overall view of the surface micromachined sidewall tribometer (a), and a detail at the beam and post where contact is made (b).

Sidewall friction structures were tested in a 24-pin package for the controlled oxygen and water vapor tests. Evaluation of supercritical CO_2-dried ($SCCO_2$) and tungsten-coated structures was performed in the ambient laboratory air environment consisting of air at 23°C and 25% relative humidity. For the controlled environment tests, packaged parts were tested in a small environmental cell that was purged with the desired environment. A sapphire window 17.8 mm in diameter in the lid allows the structures to be viewed with a microscope while they are running in the controlled environment. The free volume of the environmental cell is 250 cm^3. Dry air or nitrogen was supplied to a manifold at 10 psig, and flow meters controlled the flow of this supply gas to a desiccant column or a deionized water column. Gas exiting from these columns was mixed to generate the desired water vapor concentration. The oxygen concentration and moisture content of the environment was measured at the exit of the environmental cell using an electrochemical oxygen analyzer and chilled mirror hygrometer. The dry environments contained 1 % relative humidity (370 ppmv) or less, and the wet environments contained 40 % relative humidity (15,000 ppmv). Contact force was typically 10 μN, which is near the low end of the range of forces that can be accurately measured with the present device geometry. Devices were run at 100 Hz. The sliding distance was typically 16-24 μm per cycle (twice the track length of 8-12 μm).

2.2 Surface Coating Comparisons

Microengines

Stress tests at a drive frequency of 1720 Hz were performed on microengines with two different surface coatings. In these experiments we used samples that had either an FTS surface treatment (a fluorinated chain, perfluorodecyltrichlorosilane, $C_6F_{13}CH_2SiCl_3$)[14] or samples that were supercritical carbon-dioxide dried ($SCCO_2$). Application of a coupling agent requires preparation of the polysilicon surface by an oxidation step (H_2O_2), resulting in an oxide layer a few nanometers thick. The $SCCO_2$ samples had no specific oxidation step, but were in an air environment that would promote growth of a native oxide.

For these tests, the longitudinal force was set to 5 μN, and the microengines were run until failure. The failure criterion was defined as the inability of the gear to make a complete revolution. The microengines were produced by two separate processes that resulted in differing pin-joint gap spacing. One was 0.5 μm and the other was 0.3 μm. As shown in Figure 5, there is a difference in cycles to failure for different gap spacing. SAMS-coated microengines, which may provide some lubrication, exhibit minimal dependence of cycles to failure on gap size. However, the cycles to failure for $SCCO_2$-released microengines depends on gap size rather dramatically. Note also the opposite effects of SAMS coatings for microengines of different gap size. In the case of a 0.5 μm gap, $SCCO_2$ released microengines have a longer lifetime than SAMS-coated microengines and just the opposite is true for the 0.3 μm gap case.

Wear in a confined space such as the gap in a pin joint is a very complex problem. The majority of works on the formation and the role of wear debris/particles have been performed on "open" sliding systems. In these tests, wear particles are not trapped. Unfortunately, in our microengine, wear particles were trapped and agglomerated into larger debris, roughly 200 nm in diameter. Rabinowicz[15] shows that seizure of close-toleranced sliding components arises whenever the clearance is smaller than the largest wear particles produced by the sliding system. However, the real culprit is agglomeration of particles. Mosleh et al.[16] found that agglomeration of wear particles in bearings increased the normal load at the contact point, leading to seizure. For $SCCO_2$ dried microengines, the difference in lifetime due to gap size is far greater than the coating difference.

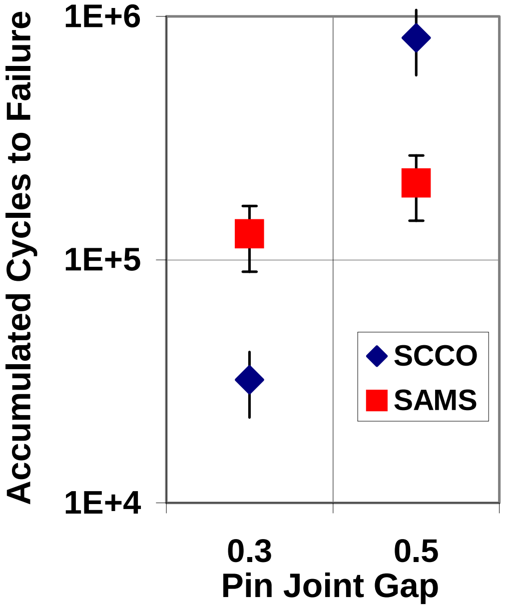

Figure 5. The effect of pin joint gap and release treatment on the lifetime of a microengine.

Friction Testers

The friction and wear behavior of uncoated friction testers was examined by testing devices that were given the normal release etch but then dried in $SCCO_2$. No additional oxidation step was performed on these samples, but they were stored in dry air and exposed to ambient air during testing, and so would contain a natural oxide layer.

The uncoated structures typically ran for less than 40 minutes, corresponding to 240,000 cycles and a total sliding distance of about 5.7 meters. The displacement during operation resulted in a friction coefficient of 0.16. This friction coefficient suggests that a layer of adsorbed hydrocarbons is providing lubrication, since friction measured between clean surfaces of silicon in prior microsystem experiments yielded a friction coefficient near 2.0.[17]

2.3 Effect of the Environment

Microengines

Humidity was shown to be a strong factor in the wear of rubbing surfaces of SAMS-coated polysilicon microengines.[18] The lifetime of the microengines was determined in separate experiments where the humidity level was varied from 1.8% RH to 65% RH at an ambient lab temperature of 23°C. It was demonstrated that very low humidity lead to very high wear without a significant change in failure lifetime.

The volume of wear debris generated is a function of the humidity in an air environment. As the humidity decreases, the wear debris generated increases. The behavior of the microengines tested at levels near 0% was quite different than those at higher levels. In the low humidity case, there was a dramatic increase in the amount of wear debris. We first noticed the formation of wear debris after accumulation of roughly 10^5 cycles. The debris was typically thrown out from the hub and collected on the gear face and surrounding substrate. In general, the gear hubs were worn down and the gears exhibited severe wobble during operation. In 55% of the failures the pin joint actually wore down and severed. We suspect that the large wear rate removes any asperities that would cause the gear to seize in the same manner as the higher humidity levels. Therefore, wear of polysilicon would continue until the pin joint is worn away, causing failure at a higher number of cycles. The wear debris generation at different humidity levels is shown in Figure 6. The microengines were stressed for roughly the same numbers of cycles, but the amount of wear debris for each case is dramatically different.

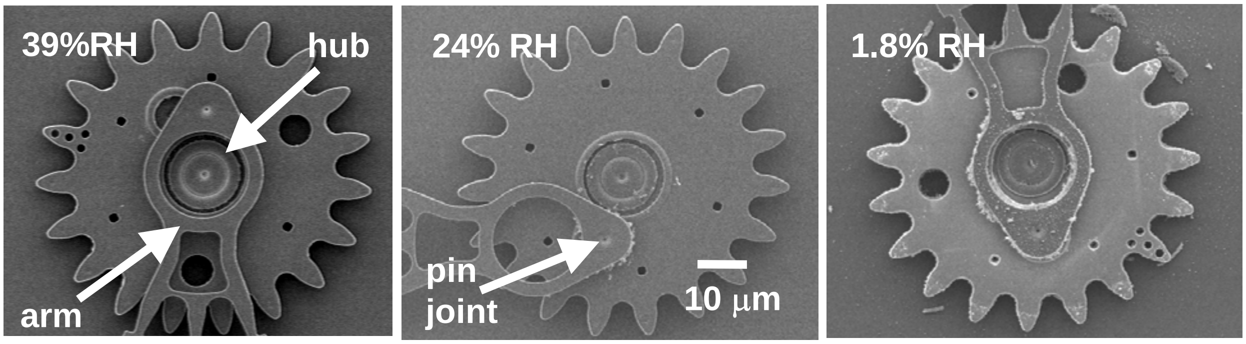

Figure 6. SEM images of various microengine gears stressed under humidity conditions of 39%, 24%, and 1.8% RH at 25° C. The microengines were stressed for roughly the same numbers of cycles.

To investigate the effect of wear, FIB (Focused Ion Beam) cross sections were cut on a sample from each humidity level. Shown in Figure 7 are cross sections taken from a control (top), 39% RH (middle), and 1.8% RH (bottom) samples. The control sample was tested for functionality, but was not stressed. Because debris is not shown in the control sample we conclude that the debris was caused by wear, not the FIB cut. The 39% RH microengine was stressed to failure at 606,000 cycles and the 1.8% RH microengine was stressed to failure at 542,000 cycles. In the 39% RH case, we observed mostly pin joint wear as shown with the notched diameter. Wear of the pin joint was accompanied by a reduction in the pin joint opening, probably due to a buildup of debris. For the 1.8% RH experiment wear was observed in both the pin joint and the hub. The pin joint eventually broke in the majority of samples tested (32 times out of 50 samples) for the 1.8% case.

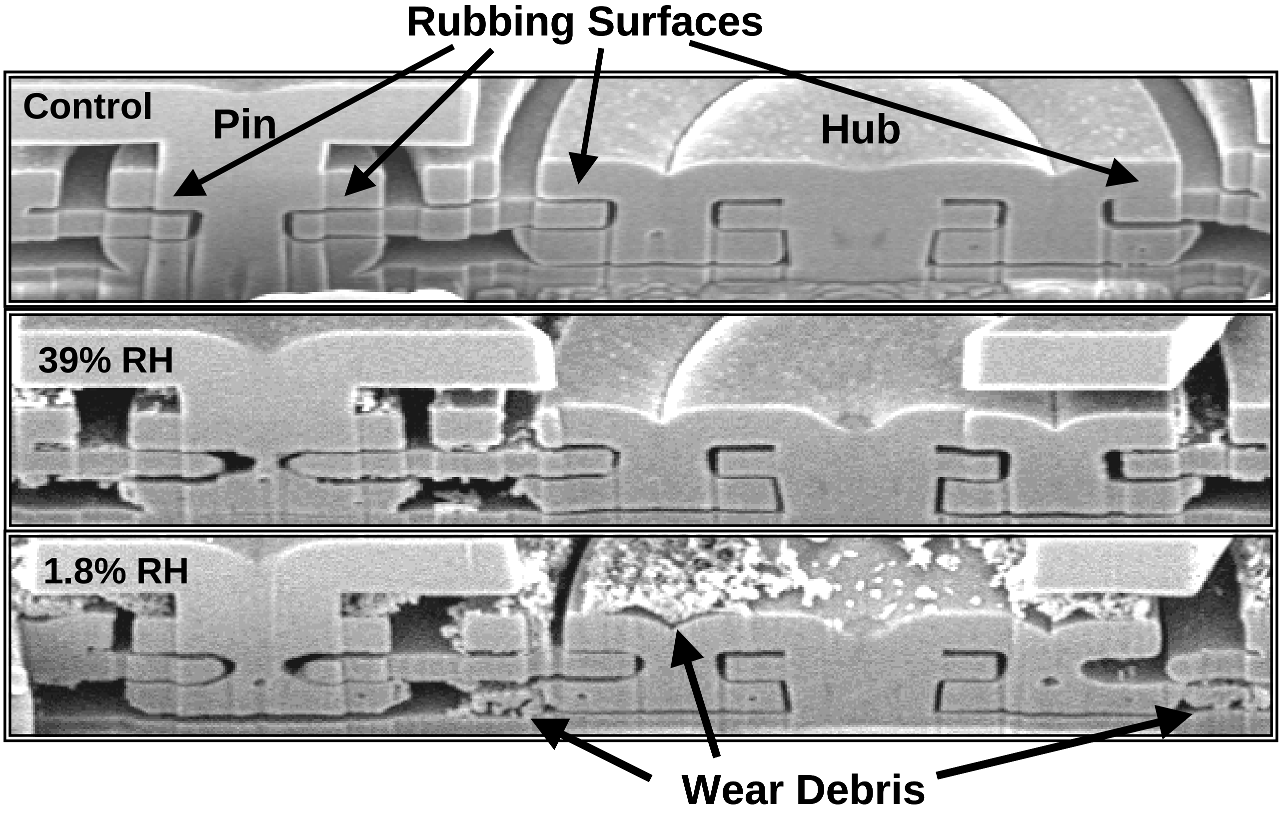

Figure 7. SEM images of an unstressed control and samples stressed at 39% RH and 1.8% RH, illustrating the amount of wear debris created in each experiment. Arrows indicate the rubbing surfaces. In both stressed samples, the pin joint has been worn down from its fabricated 3-µm diameter.

To estimate the wear volume of material one can either measure the volume of the wear debris or measure the missing volume in the worn device. We chose the latter and used the FIB cross sections from FTS-coated devices to estimate the volume worn for the humidity levels of 1.8%, 10%, 24%, and 39% RH at 25ºC.

The locations exhibiting the most wear were the hub and pin joint areas so we made our estimates there. Measurements of the diameter of worn hubs, gears, and pin joints were made. The cross sectional area was calculated and compared to the control to yield a value for worn area. This value was then multiplied by the thickness to yield the volume of the material worn away. The technique assumes that the wear is symmetrical around the hub and pin joint. We estimated the error in the technique as ± 20% of the calculated worn area. The wear volume was normalized by the total number of cycles to failure to yield wear rate, which is shown in Figure 8 as a function of % RH at 25^{o}C. Any monolayer coatings on the microengine are obviously removed as soon as debris generation begins.

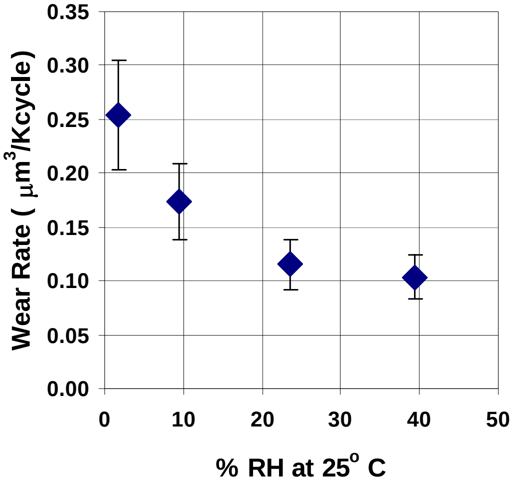

Figure 8. Wear rate of FTS-coated microengines as a function of humidity. Wear rate increases as humidity decreases.

The wear rate shown in Figure 8 agrees with studies of a SiC/SiC system[19] where the decrease in wear rate has been attributed to a tribochemical reaction leading to the formation of a protective film of hydrated amorphous silica. Silicon nitride sliding on silicon nitride was also investigated[20] and the main mechanism of wear was the tribochemical oxidation of the silicon nitride to form silicon oxide. The wear rate increased in drier conditions in the silicon nitride case also.

For the case of polysilicon sliding on polysilicon, Mizuhara and Hsu[21] reported the formation of surface hydroxides which may protect the surface from additional wear at high humidity. In this case, the mechanical wear produced dangling silicon bonds. Water reacted with this surface to form Si-OH and Si-H. Zanoria et al.[22] also reported that the rubbing-enhanced reaction of Si with water vapor generated Si-OH groups. The mechanism of Si → SiOH → SiO2 → hydrated SiO2 provided a lubricating film to protect the surface.[23]

Friction Testers

Representative behavior of the friction coefficient as a function of oscillatory cycles for the PFTS-coated friction testers is shown in Figure 9. The device run in dry air shows a low and stable friction coefficient throughout the test, with a value of 0.06 at the end of the test. This value is in good agreement with Srinivasan et al.,[15] where a friction coefficient of 0.08 was measured between PFTS-treated planar surfaces in air. The figure shows that with water vapor present, the friction behavior of the devices was erratic, with values between zero and 0.3 observed during sliding. After about 10^5 cycles, devices run in humid air would stick when the friction force exceeded the actuation force provided by the comb drives (points near μ=0.55 in the data). The device could usually be made to continue operating by briefly removing and reapplying the normal load, but would begin to stick again shortly after reapplying the load. Accumulation of material could be observed by optical microscopy in the contact region of the beam in humid environments, at the ends of the contact-sliding area. No such accumulation was observed for tests run in dry conditions.

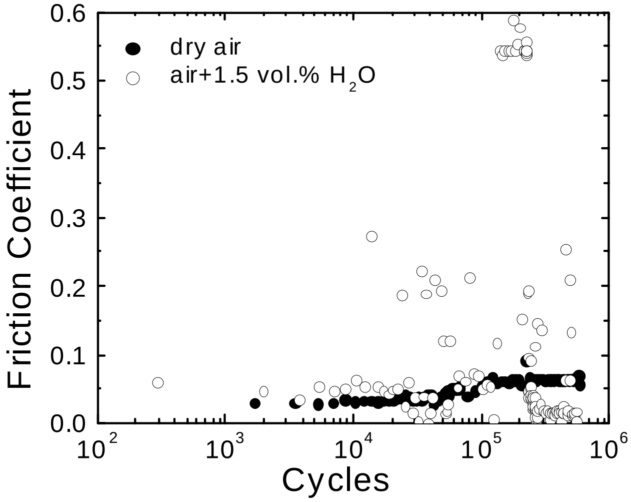

Figure 9. Friction coefficient versus cycles for PFTS-coated sidewall friction testers in dry and humid air.

The contact regions of the beam and post for tests in dry and humid air are shown in Figure 10. Scanning electron microscope micrographs of the worn surfaces from structures tested in dry air revealed very little damage or debris accumulation. A small amount of debris accumulation can be seen on the top of the beam, but very little damage has occurred to the beam surface. In contrast, the worn surface of a beam from a test in humid air shows a large amount of wear debris generation, so much so, that thinning of the beam can be seen in the image.

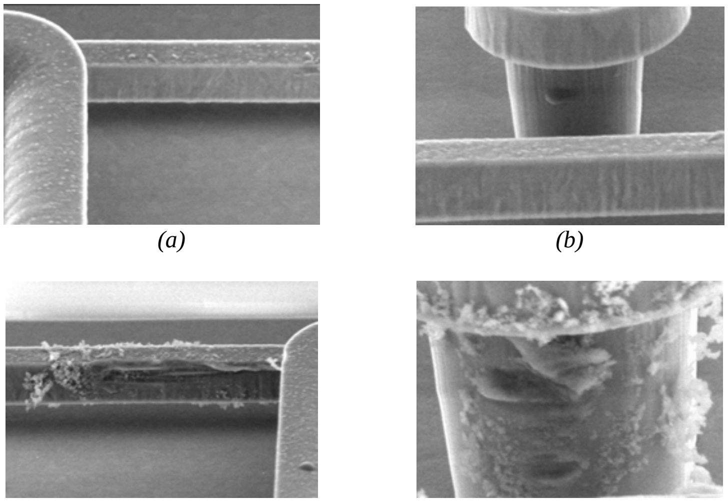
(a) *(b)*

(c) *(d)*

Figure 10. Scanning electron microscope images showing the wear surfaces on the beam (a) and post (b) of the sidewall tribometer run in dry air and humid air (c and d).

2.4 Selective Tungsten Treatment

Microengines

In order to improve the wear characteristics of devices with rubbing surfaces, a process was used to selectively coat MEMS devices with tungsten (W) using chemical vapor deposition (CVD) techniques. [24] This coating is very conformal, has excellent step coverage, and is extremely uniform. Tungsten-coated microengines tested for reliability show improved wear characteristics with longer lifetimes than polysilicon microengines.

To make a clean comparison to the polysilicon microengine, we decided to use the same drive parameters and frequency (1720 Hz) used in an earlier test. All of the earlier tests were stressed with a large longitudinal force to accelerate the time to failure. The same was done with the tungsten-coated devices.

In our earlier tests without tungsten, we observed a median time to failure of 4 x 10^5 accumulated cycles using a sample size of more than 20 microengines. This was performed in a controlled humidity environment of 39% RH. Using the same drive-signal parameters, but in ambient laboratory conditions (30-50%RH), we observed a dramatic increase in performance of tungsten-coated microengines. We saw no failures in 30 samples tested to 2 million cycles.

We have operated a number of the tungsten-coated microengines in order to determine a median time to failure. The failure distribution for devices operated in ambient air at 30-50% RH is shown in Figure 11. The median time to failure was 1.1 x 10^9 cycles with a lognormal shape parameter, σ, of 0.4. The early failure was ignored in the fit. This value can be compared directly to the $SCCO_2$ values of Figure 5 giving 3 to 4 orders of magnitude improvement. A comparison FIB cut of a polysilicon pin joint and a tungsten-coated pin joint is shown in Figure 12

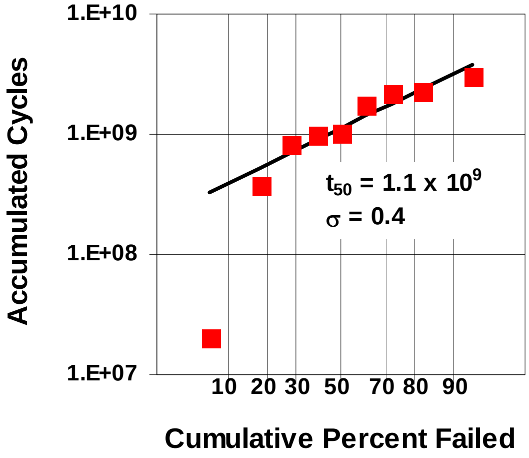

Figure 11. The lognormal distribution of 9 tungsten-coated microengine failures showing a median time to failure of 1.1 x 10^9 cycles. The early failure was ignored in the fit.

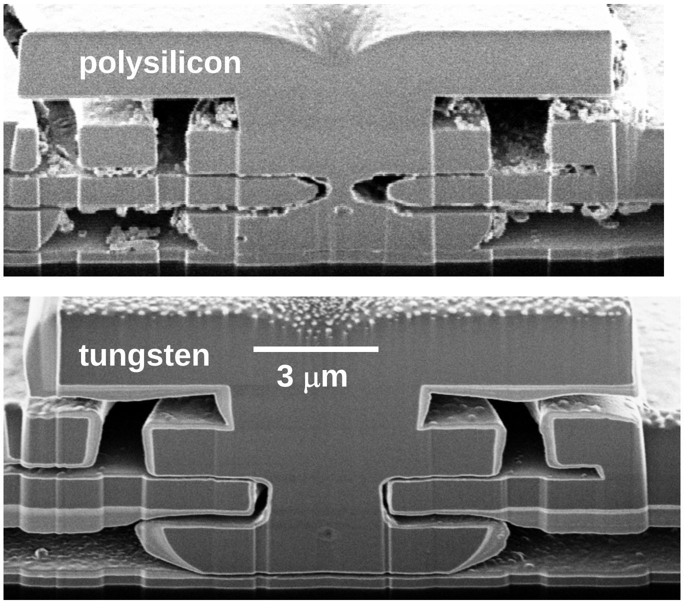

Figure 12. SEM image comparing wear in uncoated polysilicon samples and W-coated samples. The top image shows a pin joint after 607,000 accumulated cycles. Note the wear debris and the narrowing of the pin joint from its nominal 3-micron diameter. In comparison, the tungsten-coated polysilicon pin joint (bottom) shows no wear debris after 1 billion accumulated cycles.

Friction Testers

Friction coefficient as a function of oscillatory cycles for the selective tungsten coated structures is shown in Figure 13. Friction coefficient was measured with the sidewall friction structure, as described earlier. In this case, the friction coefficient remained low and consistent for the entire duration of the experiment in humid air. Contacting surfaces of the beam and post show no evidence of wear, as seen in Figure 14. X-ray photoelectron spectroscopy (XPS) was used to determine the composition of the treated surfaces as a function of time after deposition of the tungsten. Measurements of the composition of the tungsten coated surfaces, shown in Figure 15, indicate that after 14 days exposure to air (the time after which these experiments were run) the surface contains about 33 atomic percent oxygen and 17 percent W (as WO_3), 28 percent carbon, and the balance nitrogen and fluorine. While the sidewall friction tester results suggest that selective tungsten is a more wear resistant surface than the PFTS-coated silicon, the XPS data show that the oxide and a large amount of adsorbed carbon govern the tribological behavior. Additional work is needed to investigate the role of the oxide and adsorbed hydrocarbons in friction and wear for this surface treatment.

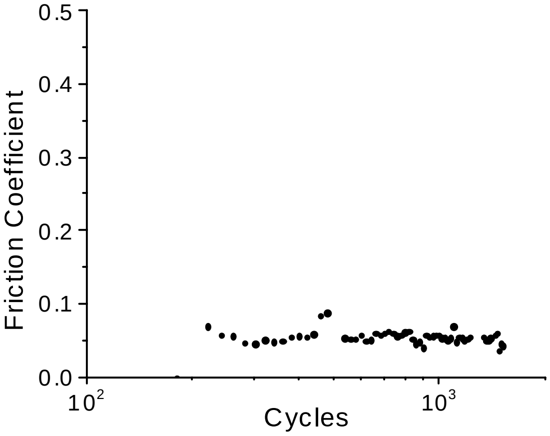

Figure 13. Friction coefficient as a function of the number of sliding cycles (one cycle = a complete forward and reverse oscillation) for a tungsten coated sidewall friction tester operated in laboratory air.

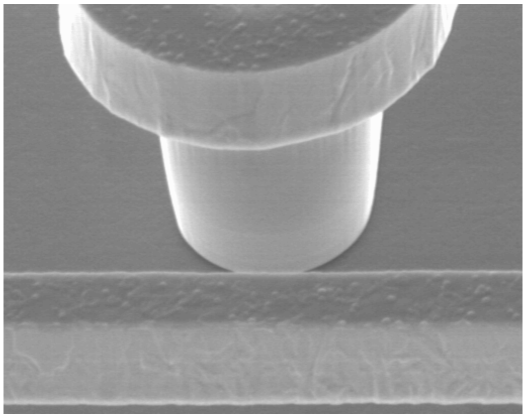

Figure 14. Scanning electron microscope image showing the wear surface on the post) of a tungsten coated sidewall tribometer.

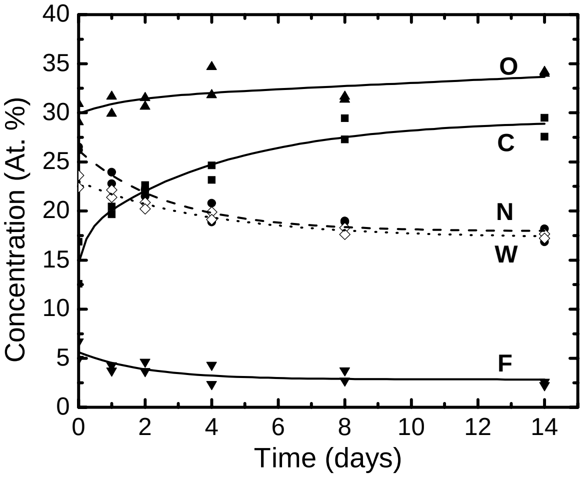

Figure 15. XPS measured composition of the selective tungsten treated surface as a function of time after treatment.

3. COMPARISONS AND BASIC UNDERSTANDING

3.1 Debris Morphology

It was shown in an earlier section (2.4) that the microengine and the friction tester had completely opposite results in dry environments. We see large amounts of wear debris in the microengine at low humidity levels and almost no wear debris in the friction tester at similar humidity levels; however, the debris morphology is similar as shown in the Figure 16. Both microengine and friction tester in this figure were run in roughly 40% RH environment at ambient temperature.

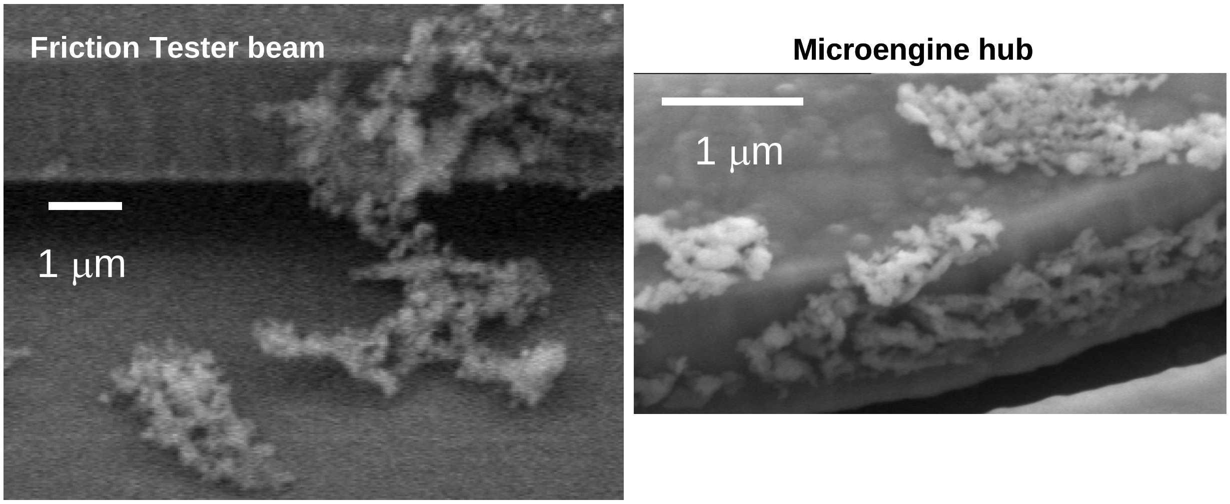

Figure 16. Wear debris generated in the friction tester and the microengine hub show similar morphology in experiments at 40% RH and ambient temperature.

Microengine

The analysis of wear debris from microengines tested in a 1.8% RH environment at ambient temperature showed the debris to be either spherical or rod-like in geometry. Figure 17a shows spherical particles ranging from 100 nm to ~250 nm in diameter. Also shown are rod-like debris particles with diameters ranging from 20 to 50 nm and lengths up to 0.5 µm. The morphology of both the spherical and rod-like structures was determined by tilting the wear debris along its axis through angles of 50^{o} to 60^{o}. These images (not shown) did not illustrate significant deviation from either the spherical or rod-like shapes.

The wear debris has been identified as amorphous oxidized silicon with either spherical or rod-like morphologies. Energy dispersive x-ray spectrums (EDS) taken from wear debris found outside the gear, adhering to the gear teeth, and inside etch release holes revealed high concentrations of carbon, oxygen and silicon. Diffraction patterns (not shown) taken from these locations showed broad ring–like patterns typical of amorphous materials. The lack of diffraction spots or speckled rings from these areas indicate no polysilicon was worn directly away from the hub or pin joint regions during testing. Figure 17b illustrates an EDS spectrum typical of debris analyzed from all three regions. High concentrations of carbon result from the thin carbon film used for sample preparation.

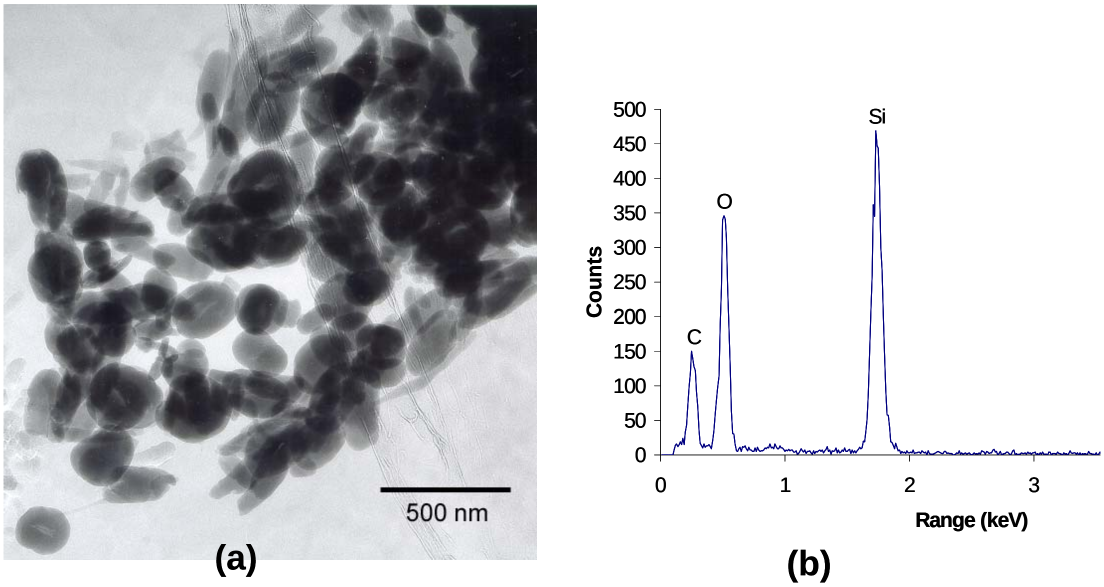

Figure 17. TEM image (a) of wear debris from a microengine tested at 1.8% RH at ambient temperature and an EDS spectrum (b) of the same debris.

Friction Testers

The chemistry and morphology of debris generated during the tests in humid environments was investigated in detail using transmission electron microscopy (TEM). In order to unambiguously identify the debris structure and composition, a probe made of a glass fiber drawn to a small diameter was used to pluck some of the debris observed in the optical microscope from the side of the beam. This debris was placed on a carbon-coated TEM grid. In addition, an electron-transparent slice was taken from the beam on the wear surface, at a location near where the beam contacts the post under static loading. A layer of platinum was deposited in-situ to fix the beam in place, and then a focused ion beam (FIB) was used to cut out a section of the beam on the worn side, so that the surface and subsurface of the beam could be examined at high resolution.

Figure 18(a) shows a debris particle sitting on a thin film of carbon. The debris is composed of particles on the order of 30 nm in diameter that have agglomerated to form a larger particle. An energy dispersive x-ray spectrum of electrons passing through the particle is shown in Figure 18(b). The particle is composed of oxidized silicon. The particle

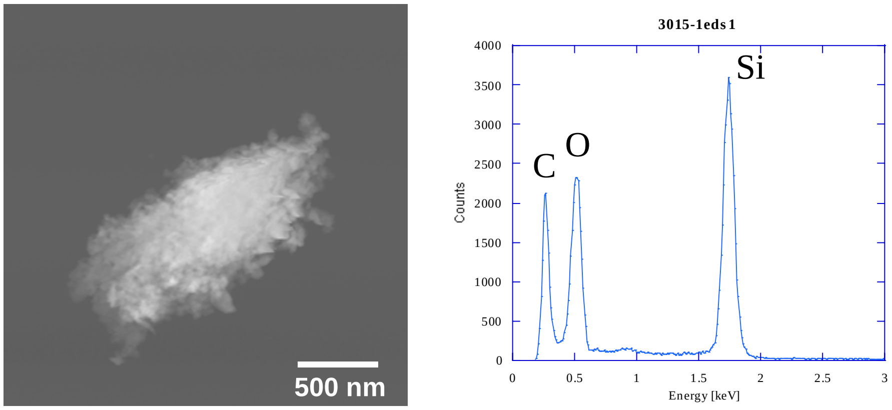

(a) (b)

Figure 18. Annular dark field TEM image (a) and energy loss spectrum (b) of debris collected from the post from a test of a PFTS-coated structure in 40% relative humidity.

produced no diffraction pattern, suggesting that the constituents are amorphous silicon oxide. It must be noted that the technique employed here should have been able to resolve individual debris particles on the order of 2-3 nm in size. However, no debris particles this small were observed. The constituent particles of ~30nm diameter that make up the agglomerates are much larger than the thickness of the natural oxide on silicon. The fact that the smallest oxide particles observed are an order of magnitude larger than the natural oxide thickness suggests that much larger oxide layers are formed during sliding contact.

Figure 19 shows an electron image and spectral image analysis of energy dispersive x-ray spectra collected at each pixel in the image. This is a multivariant analysis method that identifies all phases present in a sample by correlation of spectral data collected at each point.[25] Other than the Pt used to stabilize the beam section on the surface, and the Si in the beam, the analysis identified just one phase. This phase contained silicon and oxygen, again showing that the wear debris adhering to the worn surface is amorphous silicon oxide.

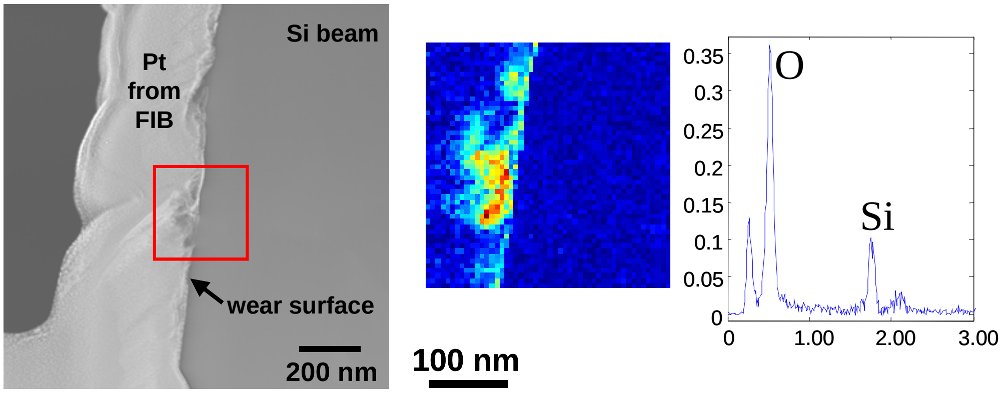

(a) (b)

Figure 19. Annular dark field TEM image (a) and energy loss spectrum (b) of debris collected from a FIB section of the beam from a test of a PFTS-coated structure in 40% relative humidity.

3.2 Failure Modes/Mechanism

We have observed wear as the failure mechanism in two different devices and many different environmental conditions, contact forces, and contact areas. Wear is a complex mechanism and in the case of the microengine, we have observed an interesting pattern. In many cases, our failure distributions were bimodal as shown in Figure 20. We observed no wear debris for the lower distributions. In many cases, analysis of failed devices with a Focused Ion Beam (FIB) showed areas of adhesion. This adhesion is representative of the first step in adhesive wear. In many cases, the force of the microengine linkage arms was sufficient to break the initial adhesion and continue operating. A continuation of this process resulted in the upper distributions of failure where we observed large amounts of wear debris. The wear debris formation introduced three-body wear, probably including abrasive wear, which lead to more wear debris. The dramatic influence of third body wear upon tribological processes is well known.[26] We are not certain if the upper distribution failures are due to an adhesion event or an accumulation of wear debris.

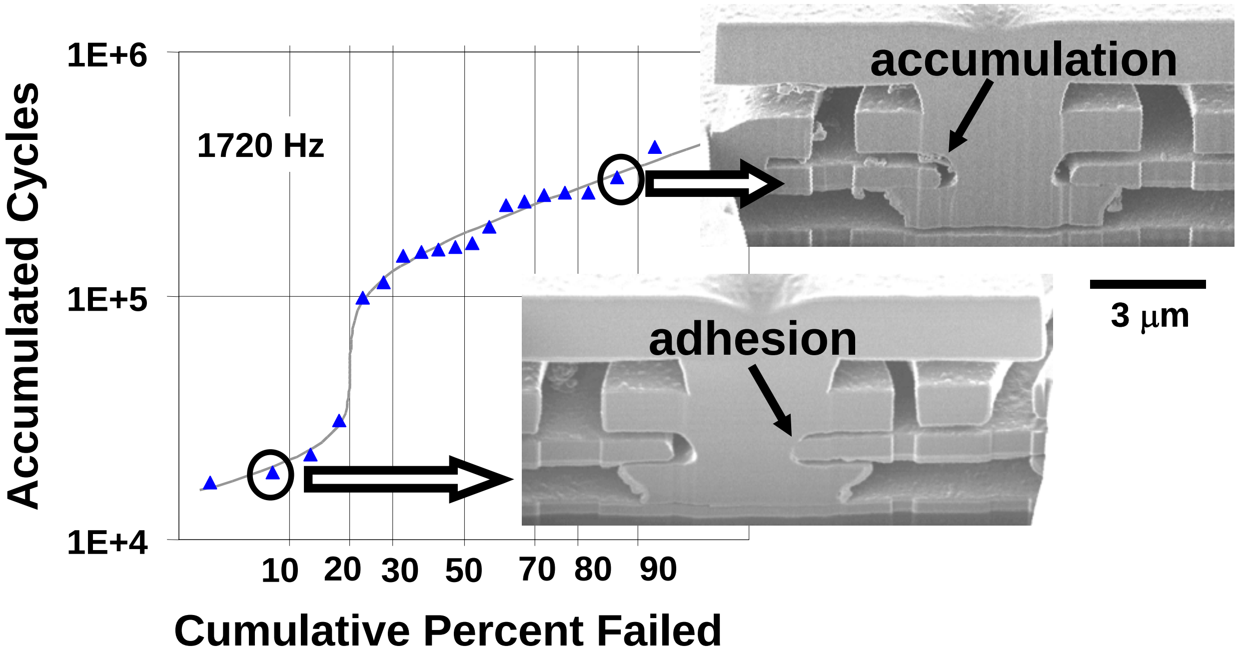

Figure 20. This bimodal distribution represents two wear failure mechanisms.

3.3 Failure Cycles

The comparison between the friction test structure and the microengine results requires that we calculate the appropriate sliding distance by each device for each cycle. The dominant failure location for the microengine was the pin-joint region. The diameter of the pin joint was 3 µm and in most cases, it rotates in a 4-µm diameter hole in the drive gear. As shown in Figure 3, the pin joint design has large areas of sliding contact. We will assume the dominant region was the normal surfaces between the pin joint and the gear. The total sliding distance per cycle is simply the circumference of the 4-µm diameter hole, which was calculated as 12.7 µm. For a 600,000-cycle test, this corresponds to a total sliding distance of 7.6 meters.

The friction test device has operating amplitude that depends upon the drive signals applied to the oscillation actuator and the friction coefficient at the beam/post interface. For the tests at 40% relative humidity, the average displacement amplitude was 8.5 µm, and for the tests in dry air it was 11.6 µm for the same drive conditions. Therefore, for the tests in Figure 9 run on the order of 600,000 cycles (1 cycle = 2 x amplitude), this corresponds to a total sliding distance of about 10.2 meters for the humid environment and 13.9 meters for the dry environment. The sliding velocity of the microengine in these experiments was 1720 Hz x 12.7 µm or 21.8 mm/s. Although the friction tester was run at 100 Hz, the waveform used to move the beam back and forth was a square wave. Detailed analysis of the drive voltage profile, and the time required to switch from one voltage level to another, suggests that the interfacial velocity during motion was on the order of 160 mm/s. This is a factor of approximately 7 faster than the microengine, although the time at rest between sliding cycles is longer by a factor of about 17 compared to the microengine.

A comparison of contact pressures reveals some differences between the microengine and the sidewall friction tester. Contact force in the friction tester is the force exerted above that needed to bend the beam into the post. For the designs tested here, the beam typically made contact with the post with 55 V on the load actuator. An additional voltage was applied to impose a contact load on the post. Since the beam moves with an amplitude of about 10 µm during test, the load also fluctuates somewhat during the test. The magnitude of this fluctuation is determined by the sliding amplitude and the length of the beam where it makes contact with the post, and is estimated at 10%. However, to ensure contact of the beam with the post throughout the complete cycle, a load larger than the minimum to bring the beam into contact with the post was used. This results in loads of 10 μN being used for testing. A simple elastic analysis of contact pressure for a cylinder against a flat surface yields a contact pressure for the friction tester under these conditions of about 230 MPa. Since the microengine hub is constrained, much smaller radial forces can be applied without risk that the pin will come out of contact with the hub. For the tests described above, the contact pressure at the pin joint is 52 to 63 MPa. Therefore, due to operating limitations and the curvature of the post in the friction tester, the contact pressures for ideal alignment of the rubbing surfaces are a factor of 4-5 higher than in the microengine. In reality, the contact pressures for both structures are probably much higher at sidewall surfaces due to imperfect vertical alignment of the rubbing surfaces.

Table 1 shows these comparisons between the microengine and friction tester. They appear to operate in different regimes with large differences in sliding velocity and contact pressure. Another contributing factor to the difference is the trapping of wear debris, which promotes three-body wear.

Table 1. Microengine and Friction Tester Wear Parameters

	Microengine	**Friction Tester**
Sliding Distance for 600,000 cycles	7.6 m	10.2 m humid/ 13.9 m dry
Sliding Distance to Failure	1.3 m for poly; 14 km for tungsten	2.3 m for humid poly dry poly and tungsten not run to failure
Sliding velocity	21.8 mm/s	160 mm/s
Contact Pressure	63 MPa	230 MPa
Wear Debris	Trapped	Not Trapped
Debris Morphology	Agglomerated amorphous silicon oxide	Agglomerated amorphous silicon oxide

3.4 Discrepancy in Environmental Effects

The differences in wear behavior between microengines and the simplified contact in the friction device can be explained in terms of the different effects water can have on the wear of oxides. Adsorbed water can react with the surface of silicon ceramics to form a hydroxide layer. This forms a low friction surface film on the oxide and can decrease wear at low contact pressures. Water may also promote stress-corrosion cracking in oxide ceramics. This occurs at high contact pressure, where debris is formed and wear rates higher than in dry air are produced. The pressure at contact points and the debris generation and trapping characteristics of the interface will therefore determine the active wear mode. It is believed that differences in contact pressure are responsible for the differences in wear behavior observed on complex microengines and the simplified contact in the friction test device discussed above. It is not yet known how the PFTS film influences the above processes, and what the degradation mechanisms of the coating are. It is clear, however, that the effect of the operating environment on friction and wear processes can change as a function of device operating conditions, and complete characterization requires measurements over a wide range of pressure and velocity.

In Figure 19, we looked for any near subsurface damage or cracking in the polysilicon beam under the wear grooves. We found no evidence for cracks or other defects immediately below the wear grooves, other than what is naturally present in the polysilicon structure away from the wear surface. This suggests that the debris generation mechanism consists of removal of small (~30nm) particles of oxide from the silicon surface, followed by agglomeration of these small particles into larger debris particles. The fact that the debris is amorphous suggests that it is not generated as crystalline particles of silicon that subsequently oxidize. The size of the particles seems too large to result simply from abrasion of a natural oxide layer. Perhaps the oxide layer is thicker due to local heating in the presence of water vapor, or due to tribochemical reactions in the contact.

Relative humidity was observed to have opposite effects on the amount of wear for the microengine and the friction tester. The presence of water vapor in the operating environment reduced the wear rate in microengine tests, and water vapor was found to cause production of copious wear debris on the friction tester. In both cases, the debris generated was composed of small, amorphous particles that agglomerated into larger particles. Also in both cases, the smallest constituent particles (~30 nm) were larger than the thickness of the natural oxide layer. While these differences are not understood, there are some important differences in operating conditions that may lead to differences in wear behavior. The apparent contact pressure used in the friction tester is a factor of 4 to 5 times greater than that at the pin joint in the microengine. The interfacial velocity in the friction tester is a factor of 7 times greater than in the pin joint in the microengine. However, the rest time between cycles in the friction tester is a factor of about 17 greater than in the pin joint of the microengine. The geometry of the contacts are also quite different: The conformal nature of the pin joint will tend to trap any debris that is generated and keep it in the contact, where it can cause third body wear. The beam and post has a more open geometry that allows debris to escape from the contact more easily.

In terms of the wear map shown in Figure 2, the contacting materials are the same so that mechanical severity of contact can be related directly to contact pressure. However, the thermal severity of contact depends upon the ability of heat generated at the contact to be transported away from the contact. A larger thermal mass of the bodies in contact would facilitate more rapid removal of heat and lower contact temperatures. The thin cross-section of the beam in the friction tester, small size of the contact area, higher interfacial velocity, and the fact that the contact area is stationary on one surface as opposed to moving on both surfaces as in the microengine, suggest that the thermal contact severity will be higher for the friction tester. Therefore, in comparing the operating regime of the microengine and friction tester, it is likely that the friction tester operates under conditions of increased mechanical and thermal contact severity compared to the microengine. This difference in operating severity could result in the two devices operating in different wear mechanism regimes, and may explain the differences in behavior observed. Additional work is under way to understand variation in wear behavior with contact severity.

4. PREDICTIVE MODEL

4.1 Frequency Dependent Wear

Most models of wear between two contacting or rubbing surfaces include the relationship between the wear volume, ΔV, and the length of the motion producing the wear, ΔL, and F, the force between the contacting surfaces. The model can be expressed as:

$$\Delta V = cF\Delta L \tag{3}$$

where c is a variable which is directly proportional to the wear coefficient and inversely proportional to the hardness of the material.

Following this general relationship for the microengine, the total length of the motion creating the wear is related to the radius of the joint, r, and the number of revolutions, R, that the engine makes by:

$$\Delta L = 2\pi rR \tag{4}$$

Bringing equations (3) and (4) together, setting ΔV to V_c, the critical volume for failure, and R to R_f, the number of revolutions to failure, and solving for R_f we get:

$$R_f = \left(\frac{1}{2\pi}\right)\left(\frac{1}{c}\right)\frac{V_c}{rF} \tag{5}$$

For a sinusoidal drive signal, the true force on the joint will vary with drive frequency, ω, as the critical frequency, ω_o, for resonance is approached. These resonant effects are present if there exists some mechanical tolerance in the joints, as is the case here. The joints have approximately 16% tolerance as measured by the total diametral gap (0.5 μm) divided by the joint size (3 μm).

In such a case, the net force on the joint will increase as the frequency approaches the critical frequency[27] and the resulting equation is:

$$R_f = \left(\frac{1}{2\pi}\right)\left(\frac{1}{c}\right)\frac{V_c}{rF_n}\left[\sqrt{\left[1-\left(\frac{\omega}{\omega_o}\right)^2\right]^2 + \left(\frac{1}{Q}\frac{\omega}{\omega_o}\right)^2}\right] \tag{6}$$

where the term in large square brackets represents a “magnification factor” caused by approach to resonance and

F_n is the nominal force applied to the joint,

Q is the quality factor of the damped harmonic mechanical system and

ω / ω_o is the ratio of the driving frequency to the resonant frequency of the system.

In order to confirm the model derived above, we compare it to actual failure data[28] and this comparison is shown in Figure 21. The solid line is the shape that we get by simply using our best estimates of the physical parameters (from Table 3) in equation (6) and adjusting the variable c to minimize χ^2. The value of c = 3.2 x 10^{-5} $\mu m^2/N$ provided the curve that best describes the data with a χ^2 of 1.5.

There are two important characteristics in the data versus model comparison. First, the agreement supports the conclusion that the failures are associated with wear and not some other physical mechanism. However, the specific wear mechanism or combinations of mechanisms are as yet undetermined. Second, the functional dependence is correct, with the model clearly predicting the decrease in the number of revolutions to failure around the resonant frequency and the increase in the number of revolutions to failure above resonant frequency.

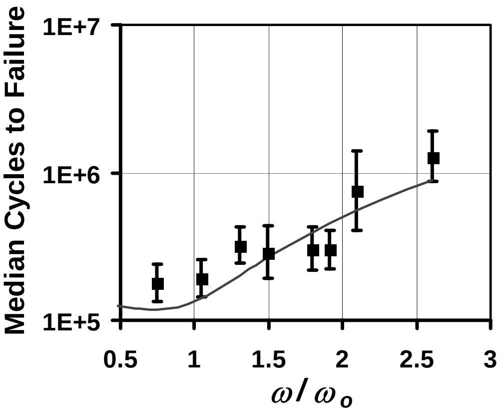

Figure 21. The frequency-dependent wear model shows good agreement with data.

4. CONCLUSIONS

We have shown that for the basic failure mechanism of wear, we could piece together the parts of our reliability methodology to develop a predictive model. Testing large numbers of devices yielded good statistical characterization of the dominant failure mechanism. Operating the test structure under the same environmental conditions revealed differences in wear mechanisms. This work will promote development of a test structure that more closely matches the device.

The lifetime of a microengine for a $SCCO_2$ – dried process was affected by the gap size with a smaller gap of 0.3 μm being the least reliable. The difference in lifetime of microengines that were SAMS coated or $SCCO_2$-dried was small, and depended on the gap size.

Although the microengine and the friction tester typically fail in the same mode due to wear, the exact failure mechanism depends on many surface interaction parameters and environmental conditions. Severe wear was observed in microengines in a dry environment, but mild wear was observed for the friction tester. Considering the wear mechanism map for ceramics, the change from severe to mild wear could be due to contact pressure or sliding velocity differences. Contributing factors include the local pressure, velocity, geometry of the contact and whether debris can be trapped, and the fact that the microengine tests are unidirectional while in the sidewall friction tester they are bi-directional.

There was complete agreement between the microengine and the friction tester using a selective tungsten coating. In both cases, no wear debris was observed. The tungsten coated friction tester was not run to failure so a comparison in cycles to failure could not be made.

ACKNOWLEDGEMENTS

The authors thank all who contributed in any way to the collection of data review here. Special thanks to Sita Mani and Jim Fleming who developed the tungsten process and Jerry Walraven who performed most of the failure analysis. We also thank Somuri Prasad and Dave Barr for careful review. We also thank the staff in the Microelectronics Development Lab who fabricated all of the devices used in these studies.

Sandia is a multiprogram laboratory operated by Sandia Corporation, a Lockheed Martin Company, for the United States Department of Energy under Contract DE-AC04-94-AL85000

REFERENCES

1. A. Hartzell and D. Wodilla, "MEMS Reliability, Characterization, and Test, Proc. Of SPIE, **4558**, 2001, pp. 1-5.
2. S. Arney, "Designing for MEMS Reliability," Materials Research Society Bulletin, April, 2001, pp. 296-299.
3. S.C. Lim and M.F. Ashby, "Wear Mechanism Maps," *Acta Metallurgica*, **35**, 1987, pp. 1-24.
4. K. Adachi, K. Kato and N. Chen, "Wear Map of Ceramics," *Wear*, **203-204**, pp. 291-301.
5. T.E. Fischer and W.M. Mullins, "Relation Between Surface Chemistry and Tribology of Ceramics," in *Friction and Wear of Ceramics*, S. Jahanmir, ed., Marcel Dekker, Inc., New York, NY (1994) pp. 51-60.
6. K. J. Gabriel, F. Behi, and R. Mahadevan, "In situ Friction and Wear Measurements in Integrated Polysilicon Mechanisms," *Sensors and Actuators,* **A21-A23**, 1990, pp. 184-188.
7. M. Mehregany, K. J. Gabriel, and W. S. N. Trimmer, "Integrated fabrication of polysilicon mechanisms," *IEEE Trans. Electron Devices,* **ED-35**, 1999, pp. 719-723.
8. Lee S. Tavrow, Stephen F. Bart, and Jeffrey H. Lang, "Operational characteristics of microfabricated electric motors," *Sensors and Actuators,* **A35**, 1992, pp. 33-44.
9. S. L. Miller, J. J. Sniegowski, G. LaVigne, and P. J. McWhorter, "Performance tradeoffs for a surface micromachined microengine," *Proceedings of SPIE Micromachined Devices and Components II*, **Vol. 2882**, Austin, October. 14-15, 1996, pp. 182-191.
10. N. F. Smith, D. M. Tanner, G. F. LaVigne, S. L. Miller, W. P. Eaton, L. W. Irwin, "Super μDriver V1.0," copyright, 1998.
11. D. M. Tanner et al., "MEMS Reliability: Infrastructure, Test Structures, Experiments, and Failure Modes," *Sandia Report*, SAND2000-0091, January, 2000, pp. 155-157. Download from http://www.prod.sandia.gov/cgi-bin/techlib/access-control.pl/2000/000091.pdf
12. D. M. Tanner, J. A. Walraven, Seethambal S. Mani, and Scot E. Swanson, "Pin-Joint Design Effect on the Reliability of a Polysilicon Microengine," *Proceedings of IRPS*, 2002, pp. 122-129.
13. W. P. Eaton, N. F. Smith, L. Irwin, D. M. Tanner, J. J. Allen, S. L. Miller, and W. M. Miller, "Characterization Techniques for Surface-Micromachined Microengines," *SPIE's 1998 Symposium on Micromachining and Microfabrication*, Santa Clara, CA, **Vol. 3514**, pp. 171-178.
14. R. L. Alley, R. T. Howe, and K. Komvopoulos, "The effect of release-etch processing on surface microstructure stiction," *Proceedings of the IEEE Solid-State Sensor and Actuator Workshop,* Hilton Head, SC, 1992, pp. 202-207.
15. E. Rabinowicz, *Friction and Wear of Materials*, John Wiley & Sons, Inc., 1995, pp.143-190.
16. M. Mosleh, N. Saka, and N. P. Suh, "A mechanism of high friction in dry sliding bearings," *Wear*, **252**, 2002, pp.1-8.
17. U. Srinivasan, J.D. Foster, U. Habib, R.T. Howe, and R. Maboudian, D.C. Senft and M.T. Dugger, "Lubrication Of Polysilicon Micromechanisms With Self-assembled Monolayers," *Proc. IEEE Solid-State Sensor Actuator Workshop,* Hilton Head, SC, USA, 1998, pp.156-161.
18. Danelle M. Tanner, Jeremy A. Walraven, Lloyd W. Irwin, Michael T. Dugger, Norman F. Smith, William M. Miller, and Samuel L. Miller, "The Effect of Humidity on the Reliability of a Surface Micromachined Microengine," Proc. of IEEE International Reliability Physics Symposium, 1999, pp. 189-197.
19. J. Takadoum, Z. Zsiga, M. Ben Rhouma, and C. Roques-Carmes, "Correlation between friction coefficient and wear mechanism of SiC/SiC system," *Journal of Material Science Letters,* **13,** 1994, pp. 474-476.
20. M. G. Gee and D. Butterfield, "The combined effect of speed and humidity on the wear and friction of silicon nitride," *Wear,* **162-164,** 1993, pp. 234–245.
21. K. Mizuhara and S. M. Hsu, "Tribochemical Reaction of Oxygen and Water on Silicon Surfaces," *Wear Particles,* Elsevier Science Publishers (D. Dowson et. al. Editors), 1992, pp. 323-328.

22. E. S. Zanoria, S. Danyluk, and M. J. McNallan, “Formation of Cylindrical Sliding-Wear Debris on Silicon in Humid Conditions and Elevated Temperatures,” *Tribology Transactions,* **38**, 1995, pp.721-727.
23. M. N. Gardos, “Advantages and Limitations of Silicon as a Bearing Material for MEMS Applications,” *Tribology Issues and Opportunities in MEMS,* Kluwer Academic Publishers, Netherlands, ed. by B. Bhushan, 1998, pp. 341-365.
24. S. S. Mani, J. G. Fleming, J. A. Walraven, J. J. Sniegowski, M P. de Boer, L. W. Irwin, D. M. Tanner, D. A. LaVan, M. T. Dugger, J. Jakubczak, and W. M. Miller, “*Effect of W Coating on Microengine Performance,*” Proceedings of IRPS, 2000, pp.146-151.
25. P.G. Kotula, M.R. Keenan and J.R. Michael, “Automated Analysis of SEM X-Ray Spectrum Images: A Powerful New Microanalysis Tool,” accepted for publication in Microscopy and Microanalysis, 2003.
26. Irwin L. Singer, “How Third-Body Processes Affect Friction and Wear,” *MRS Bulletin*, **Vol. 23**, No. 6, June 1998.
27. C. R. Freberg and E. N. Kemler, *Elements of Mechanical Vibration, 2nd ed.,* New York, John Wiley & Sons, Inc., 1949.
28. D. M. Tanner, W. M. Miller, K. A. Peterson, M. T. Dugger, W. P. Eaton, L. W. Irwin, D. C. Senft, N. F. Smith, P. Tangyunyong, and S. L. Miller, “Frequency Dependence of the Lifetime of a Surface Micromachined Microengine Driving a Load,” in *Microelectronics Reliability Journal*, **39** (1999) pp. 401-414.

.